Improvements to the Blade Element Momentum Formulation of OpenFAST for Skewed Inflows

Journal of Physics: Conference Series **2767** (2024) 022003 doi:10.1088/1742-6596/2767/2/022003

Improvements to the Blade Element Momentum Formulation of OpenFAST for Skewed Inflows

E. Branlard[1], J. Jonkman[2], B. Lee[2], B. Jonkman[3], M. Singh[3], E. Mayda[3], K. Dixon[3]

[1]University of Massachusetts Amherst, Amherst, MA, USA
[2]National Renewable Energy Laboratory, Golden, CO, USA
[3]Envision Energy, Boulder, CO, USA

E-mail: ebranlard@umass.edu

Abstract. In this work, we modify the blade element momentum algorithm of OpenFAST to improve its predictions under large skewed inflow conditions. We use the well-known Glauert's skew correction and introduce continuous extension of the model for high-thrust conditions. We present the rationale behind Glauert's empirical model and discuss the different conventions possible for the axial induction factor. We verify the model against the higher-fidelity lifting-line vortex method and blade-resolved computational fluid dynamics, and we observe that the new implementation enhances the accuracy and reliability of OpenFAST's aerodynamic modeling capabilities in conditions involving large skew angles. For the parametric studies run using the different codes, we find that the power changes with the skew angle as $\cos^{1.7}(\theta_{\text{skew}})$ and the thrust as $\cos^{0.65}(\theta_{\text{skew}})$. An analysis of the azimuthal variation of the induced velocities in the rotor plane reveals that current redistribution models used in blade element momentum codes may need to be refined.

1. Introduction

The multiphysics engineering tool OpenFAST models the aerodynamics of wind turbines through the AeroDyn module [1]. This aerodynamic module includes, among others, a blade element momentum (BEM) algorithm to compute the loads and induced velocities on rotating blades. The present BEM algorithm was introduced in 2014 [2], and its core has received limited changes since. Recent verification and validation work (e.g., [3]) has revealed weaknesses in the formulation in cases with large skew angles. Skew refers to the case where the main inflow is not perpendicular to the rotor plane but at a given angle of incidence. For a wind turbine, both tilting and yawing of the nacelle introduce skew. Under uniform inflow, situations with pure yaw, pure tilt, or a combination of the two are aerodynamically equivalent when expressed in a suitable coordinate system.

In this work, we present changes to the AeroDyn algorithm to improve the predictions at large skew angles, and we compare the old and new formulations of AeroDyn against blade-resolved computational fluid dynamics (CFD) simulations and vortex-wake simulations.

Skew models for BEM codes typically consist of three components: a momentum correction, a modification of the high-thrust correction, and a redistribution of the induced velocities. In this work, we revise the first two aspects of the OpenFAST formulation that were previously missing:

(i) We reformulate the momentum theory model to include skewed inflow effects on the momentum balance, referred to as the "skew momentum theory."
(ii) We modify the high-thrust correction algorithm such that it is a function of the skew angle.

We detail these models in the following sections before presenting results in section 4.

2. Skew momentum correction

2.1. Glauert's empirical formula

In 1926, Glauert [4] suggested a model to account for the change of thrust of a rotor when placed at an angle of incidence (skew angle) relative to the wind. The model is empirical and not derived from first principles. The model can be justified by considering the skewed situation as an intermediate between an aligned flow and a fully skewed flow. The notations for the three cases are illustrated in Figure 1. For aligned flows of a rotor (Figure 1, left), the one-dimensional

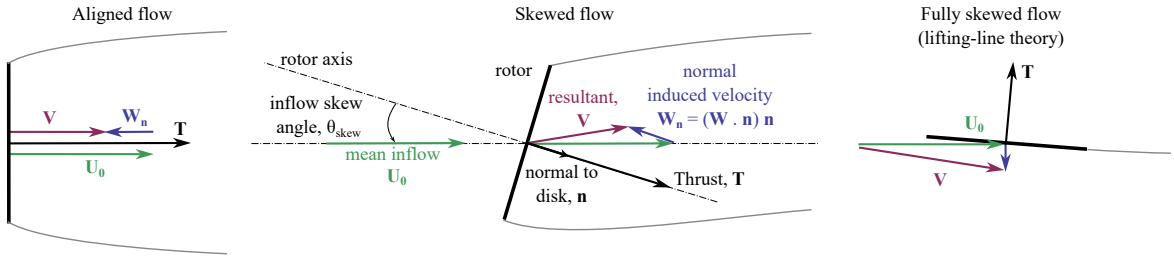

Figure 1. Notations for Glauert's empirical skew momentum correction. The flow about a skewed rotor (center) is seen as an intermediate between aligned flow (left) and fully skewed flow (right).

axial momentum theory [5, 6, 7] gives

$$T = 2\rho S \|\boldsymbol{U}_0 + \boldsymbol{W}_n\| \, \|\boldsymbol{W}_n\| \qquad \text{(aligned)} \tag{1}$$

where bold symbols are vectors, ρ is the air density, S is the rotor area, $\boldsymbol{U}_0$ is the freestream velocity, and $\boldsymbol{W}_n$ is the induced velocity normal to the rotor plane. In general, we define the induced velocity vector, $\boldsymbol{W}$, and the unit vector normal to the rotor plane, $\boldsymbol{n}$, such that by definition, $\boldsymbol{W}_n = (\boldsymbol{W} \cdot \boldsymbol{n})\boldsymbol{n}$. In aligned flows, the axial induction factor, a, is defined such that $\boldsymbol{W}_n = -aU_0\hat{\boldsymbol{x}}$, where $\hat{\boldsymbol{x}}$ is the unit vector along the main flow. After introducing the induction factor into Equation 1, the thrust coefficient is obtained as $C_T = 2T/(\rho S U_0^2) = 4a(1-a)$, which is the classical result of wind turbine axial momentum theory.

When the rotor is skewed to almost 90° (Figure 1, right), the flow can be assumed to resemble the one about a wing. Using Glauert's expansion of Prandlt's lifting-line theory [8, 9], the lift on a wing, under the small angle approximation, is obtained as

$$T = \frac{1}{2}\rho U_0^2 \pi S \mathbb{AR} A_1 \tag{2}$$

where S is the wing surface, $\mathbb{AR}$ is the wing aspect ratio (as computed in the classical lifting-line theory: $\mathbb{AR} = b^2/S$, with b the wing span), and A_1 is the first coefficient of Glauert's expansion, which involves expressing the circulation, Γ, as a Fourier series: $\Gamma = 2U_0 b \sum_{n\geq 1} A_n \sin(n\theta_y)$, where the angle θ_y is defined as $\cos\theta_y = -2y/b$, with y as the axis along the wing span. For a circle (or an ellipse), the aspect ratio is $\mathbb{AR} = 4/\pi$ (and not 1 if a different convention were used). Assuming an elliptic distribution of the circulation, $\Gamma = \Gamma_{\max}\sqrt{1 - 4y^2/b^2}$, the only coefficient in Glauert's expansion is A_1 because $\sqrt{1 - 4y^2/b^2} = \sin\theta_y$ by definition. The maximum circulation is then identified as $\Gamma_{\max} = 2U_0 b A_1$. In the special case of an elliptic distribution of the

circulation, lifting-line theory predicts an induced velocity equal to $\|\boldsymbol{W}_n\| = \Gamma_{\max}/(2b) = U_0 A_1$. Inserting this definition into Equation 2 leads to

$$T = 2\rho S U_0^2 A_1 = 2\rho S \|\boldsymbol{U}_0\| \, \|\boldsymbol{W}_n\| \approx 2\rho S \|\boldsymbol{U}_0 + \boldsymbol{W}_n\| \, \|\boldsymbol{W}_n\| \qquad \text{(fully skewed)} \qquad (3)$$

where the approximation above is valid under the small angle approximation of the lifting-line theory. It is the analogy between Equation 1 and Equation 2, obtained for the two extreme situations of aligned flows and fully skewed flows, that led Glauert to assume that the form taken by these equations can be expected to be valid for intermediate flows. Glauert's empirical skew momentum correction therefore consists of using Equation 1 for skewed flows (Figure 1, center).

2.2. Local formulation for BEM implementation

In this work, we assume that Glauert's skew momentum equation is also valid at the annulus level, that is, for an elementary thrust, $\mathrm{d}T$, spread over an annulus of area $\mathrm{d}S$. This is also the approach mentioned in other references [10, 11]. We further assume that the local thrust on a blade node can be obtained from the annulus thrust by multiplication with Prandtl's tip-loss factor, F. The local thrust is therefore taken as

$$\mathrm{d}T = 2\rho \, \mathrm{d}S \, F \|\boldsymbol{U}_0 + (\boldsymbol{W} \cdot \boldsymbol{n})\boldsymbol{n}\|(-\boldsymbol{W} \cdot \boldsymbol{n}) \qquad (4)$$

where $\boldsymbol{U}_0(r, \psi)$ and $\boldsymbol{W}(r, \psi)$ are the local wind and induced velocity taken at radial position r along one of the wind turbine blades at azimuthal position ψ. The notation (r, ψ) is omitted for conciseness. The projection of the wind against the rotor normal (see Figure 1, center) is: $U_n = \boldsymbol{U}_0 \cdot \boldsymbol{n} = U_0 \cos\theta_{\text{skew}}$. We define the axial induction factor, a, using the wind normal to the rotor[1]; therefore,

$$\boldsymbol{W} \cdot \boldsymbol{n} = -aU_n = -aU_0 \cos\theta_{\text{skew}} \qquad (5)$$

Using the definition from Equation 5, Equation 4 becomes

$$\mathrm{d}T = \frac{1}{2}\rho (U_0 \cos\theta_{\text{skew}})^2 \, \mathrm{d}S \, 4aF\sqrt{(1-a)^2 + \tan^2\theta_{\text{skew}}} \qquad (6)$$

We also define the local thrust coefficient, $C_{t,\text{MT}}$ (for momentum theory), as function of the wind normal to the rotor; therefore,

$$C_{t,\text{MT}} = \frac{\mathrm{d}T}{\frac{1}{2}\rho (U_0 \cos\theta_{\text{skew}})^2 \, \mathrm{d}S} = 4aF\sqrt{(1-a)^2 + \tan\theta_{\text{skew}}} \qquad (7)$$

We note that different formulations are obtained if the axial induction factor and the thrust coefficients are defined with U_0 instead of U_n (see Appendix A). Equation 7 is illustrated on the left of Figure 2 for a tip-loss factor of 1. We observe that, for a given thrust coefficient, the axial induction factor is reduced when the skew angle increases. This observation is also true when these quantities are expressed as a function of U_0 (see Appendix A). The previous AeroDyn implementation did not account for this dependency with the skew angle and, as will be shown in section 4, was therefore predicting inductions that were too high.

2.3. BEM equations

The BEM equations are obtained by equating the local thrust[2] coefficients from MT and blade element theory (labeled BT in the following). The local thrust coefficient from BT takes the

[1] We present results for a different convention in Appendix A.

[2] The torque coefficients from both theories also need to be equated. Typically, the thrust equation is used to determine the axial induction and the torque equation for the tangential induction. This is the approach used here.

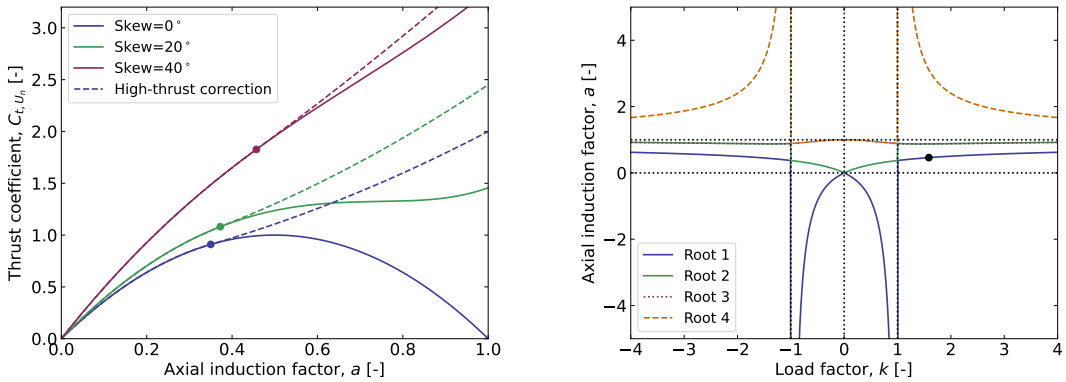

Figure 2. Left: Skew momentum theory (Equation 7) and high thrust correction (Equation 13). Dots represent the value at $a = a_c$. Right: The four roots of the $k-a$ relationship (Equation 10), for $\theta_{\text{skew}} = 40°$.

following form [9]:

$$C_{t,\text{BT}} = 4Fk(1-a)^2, \qquad \text{with} \quad k = \frac{\sigma c_n}{4F} \frac{{}^{a}V_{\text{rel}}^2}{U_n^2(1-a)^2} \frac{\mathrm{d}z}{\mathrm{d}r} \tag{8}$$

where ${}^{a}V_{\text{rel}}$ is the relative velocity norm in the airfoil coordinate system, c_n is the aerodynamic coefficient (based on the angle of attack in the airfoil system) projected along $\boldsymbol{n}$, σ is the local solidity, z is the spanwise coordinate along the pitch axis of the blade, and r is the radial coordinate in the rotor plane. The BEM equations are obtained by equating Equation 7 and Equation 8. ${}^{a}V_{\text{rel}}$ depends on the axial and tangential induction, the elastic motion of the blade, the airfoil aerodynamics, and the geometrical transformation between the coordinate system of the MT (typically the rotor plane) and BT (typically the airfoil chord). The problem of solving for the axial induction is therefore nonlinear and can be solved using different methods (see e.g., [12] for a straight blade), the most common ones being the iterative method of rearrangement (used, e.g., in [10, 9]) and the method of Ning [2]. In this work, we use the method of Ning to express the BEM equations as a constraint based on the flow angle as variable, but we internally solve for the axial induction using the approach described below. The approach can also be used in other methods of solutions such as the iterative method.

We begin by equating Equation 7 and Equation 8:

$$k(1-a)^2 = a\sqrt{(1-a)^2 + \tan\theta_{\text{skew}}}, \qquad \left(\text{alt.} \quad k = \frac{a}{|1-a|}\sqrt{1 + \frac{\tan\theta_{\text{skew}}}{(1-a)^2}}\right) \tag{9}$$

where an alternative form is presented on the left for future use. Then, we square the equation to remove the square root, and obtain

$$(1-k^2)a^4 + (4k^2-2)a^3 + (-6k^2 + \tan^2\theta_{\text{skew}} + 1)a^2 + 4k^2a - k^2 = 0 \tag{10}$$

This quartic equation can be solved to find the axial induction factor that corresponds to a given value of k. The algorithm is by nature iterative because k depends on a. We note that the typical solution without skew and in the windmill state is $a = k/(1+k)$, or equivalently, $k = a/(1-a)$, which is often used in iterative BEM algorithms. The four roots of Equation 10 are illustrated on the right of Figure 2. We choose between the roots based on the loading state of the rotor (e.g., "windmill" or propeller states) and the sign of the flow angle. Most "windmill" operation occurs for $k \geq 0$ and $a \geq 0$, and typically the first and second roots are used. For high loading and high axial induction factors, a correction is used, as detailed in the next section.

3. High-thrust correction and skew

High-thrust corrections are used in BEM codes to alleviate the so-called momentum breakdown, where momentum theory predicts a zero or negative velocity in the wake for axial induction factors larger than $a = 0.5$. Corrections have been developed for aligned rotors and therefore need to be corrected for rotors in skew. We introduce a critical axial induction value, a_c, indicated by dots on Figure 2, above which an empirical high-thrust correction should be applied. For aligned flows, the value $a_c = 0.35$ is used by AeroDyn. For skewed flows, we empirically suggest the following model:

$$a_c = \min\left[\frac{0.35}{\cos\theta_{\text{skew}}}, \frac{1}{2}\right] \tag{11}$$

Using Equation 9, this critical value corresponds to a critical value of k equal to

$$k_c = \frac{a_c}{|1-a_c|}\sqrt{1+\frac{\tan\theta_{\text{skew}}}{(1-a_c)^2}} \tag{12}$$

It is common to represent high-thrust corrections using a polynomial; for example, Spera used a first-order polynomial [9], Glauert used a second-order polynomial [9], and a third-order polynomial is found in the $a(C_t)$ relationship of Madsen et al. [11]. In line with the previous version of AeroDyn, we use a second-order polynomial:

$$C_{t,\text{HT}}(a) = c_2 a^2 + c_1 a + c_0 \tag{13}$$

where the label HT is used for "high-thrust." As illustrated in Figure 3, we ensure C^1-continuity between the momentum theory and the polynomial extension at $a = a_c$. This leads to two

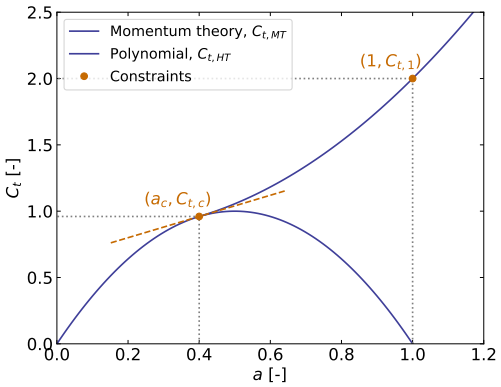

Figure 3. Second-order polynomial obtained as C^1 continuation of the momentum theory relation and using an additional constraint at $a = 1$.

constraints:

$$C_{t,\text{HT}}(a=a_c) = C_{t,c} = C_{t,\text{MT}}(a=a_c), \qquad \frac{dC_{t,\text{HT}}}{da}(a=a_c) = s_c = \frac{dC_{t,\text{MT}}}{da}(a=a_c), \tag{14}$$

where $C_{t,c}$ and s_c are the value and slope of C_t at the critical point a_c. We introduce the third constraint by specifying an empirical value at $a = 1$. Currently, this value is set as follows:

$$C_{t,\text{HT}}(a=1) = C_{t,1} = \max\left[2 + 2.113\sqrt{(\tan\theta_{\text{skew}})}, C_{t,c} + s_c(1-a_c)\right] \tag{15}$$

The maximum is introduced to ensure that the polynomial extension is above the tangent at a_c. Different empirical models may be used in the future based on supporting experiments. With

these three constraints, the coefficients in Equation 13 are entirely determined as

$$c_0 = (1-a_c)^{-2}(C_{t,1}a_c^2 - 2C_{t,c}a_c + C_{t,c} + a_c^2 s_c - a_c s_c), \tag{16}$$

$$c_1 = (1-a_c)^{-2}(-2C_{t,1}a_c + 2C_{t,c}a_c - a_c^2 s_c + s_c), \tag{17}$$

$$c_2 = (1-a_c)^{-2}(C_{t,1} - C_{t,c} + a_c s_c - s_c). \tag{18}$$

The high-thrust corrections for different skew angles are illustrated in the left of Figure 2.

We adapt the method of solution presented in subsection 2.3 to obtain a for high loading conditions. We equate the C_t from HT (Equation 13) with the one from BT (Equation 8), leading to the following quartic equation:

$$(A^2 - c_2^2)a^4 - (4A^2 + 2c_1c_2)a^3 + (6A^2 - 2c_0c_2 - c_1^2)a^2 - (4A^2 + 2c_0c_1)a + (A^2 - c_0^2) = 0 \tag{19}$$

with $A = 4kF$. Equation 10 is used when $k \leq k_c$ (or, equivalently, $a \leq a_c$). Equation 19 is used otherwise.

4. Results

We implemented the two models described in section 2 and section 3 in the BEM module of AeroDyn. In this section, we present results of the old and new BEM of AeroDyn (labeled "BEM-old" and "BEM-new") against free-wake vortex-lattice simulations performed using the OLAF module of AeroDyn [13] and blade-resolved CFD using the ExaWind framework [14].

4.1. Simulation setup

We use the International Energy Agency Wind Technology Collaboration Programme 15-MW reference wind turbine [15] as a baseline model. We use the test case suggested in an open-source benchmark[3] intended to compare aeroelastic codes. The baseline model is modified to remove precone, prebend, presweep, and tilt, and it uses 51 equidistant blade stations. The operating conditions are chosen such as to be in Region 2 (optimal C_p tracking region), with a uniform wind speed set to $U_0 = 9$ m/s (no turbulence or shear). The rotational speed is prescribed at $\Omega = 6.4$ rpm and the pitch at 0° for all cases. In aligned flows, this corresponds to a tip-speed ratio of $\lambda = 9$, and gives aerodynamic coefficients of $C_T = 0.78$ and $C_P = 0.48$. For the BEM and vortex code (further referred as "lifting-line" codes), we updated the baseline airfoil polars and used polars obtained from a two-dimensional version of the CFD solver at Reynolds numbers 3, 5, 8, 10, and 15 million.

The OLAF parameters were set such that vorticity is shed every 6° of azimuth; the wake performs five free revolutions and 11 revolutions with a frozen wake, resulting in a wake length of approximately 5 rotor diameters; and the blade and wake regularization is set to 0.35 and 0.25 of the blade chord.

Blade-resolved CFD simulations were performed using the ExaWind stack [14]. Nalu-Wind, an unstructured mesh-based solver, was employed for near-body (blade) simulations, and AMR-Wind, a Cartesian mesh-based solver, was applied for off-body simulations. Overset connectivity between Nalu-Wind and AMR-Wind meshes was searched through TIOGA. All cases shared the same AMR-Wind setup, and the Nalu-Wind mesh was rotated based on yaw angles. The simulations were run for 15 rotor revolutions with a time step size of 0.125°, and the integrated rotor performance was calculated by averaging over the last revolution. The k–ω SST turbulence model was utilized for turbulence closure in both Nalu-Wind and AMR-Wind. The rotor mesh (Nalu-Wind) comprises 17 million cells (one third per blade), and the background mesh (AMR-Wind) is composed of 30 million cells, for total 47 million cells.

For each code, we run parametric studies by varying the yaw (skew) angle from -50° to 50°. For BEM and OLAF, parametric tilt studies were also performed to verify that the results are

[3] `https://github.com/ebranlard/aerobench` (accessed Nov. 2023, commit: df1c2ae)

the same between pure yaw and pure tilt. We also performed these parametric studies with the National Renewable Energy Laboratory's 5-MW turbine and found similar conclusions as those presented in the subsequent sections with similar accuracy; therefore, these results are not included for conciseness. We expect the model to perform well for common turbine designs, but it remains to be investigated whether nonlinear effects are present for blades with large prebend or presweep operating in large skew.

The average simulation times for simulating 10 min is 10 s for BEM (on one core), 20 min for OLAF (on 12 cores), and 96 hours (on 1440 cores) for the blade resolved CFD.

4.2. Integral quantities

In the left of Figure 4, we show the power and thrust obtained using BEM formulations, vortex methods, and CFD for varying yaw angles. We observe that the results from the old

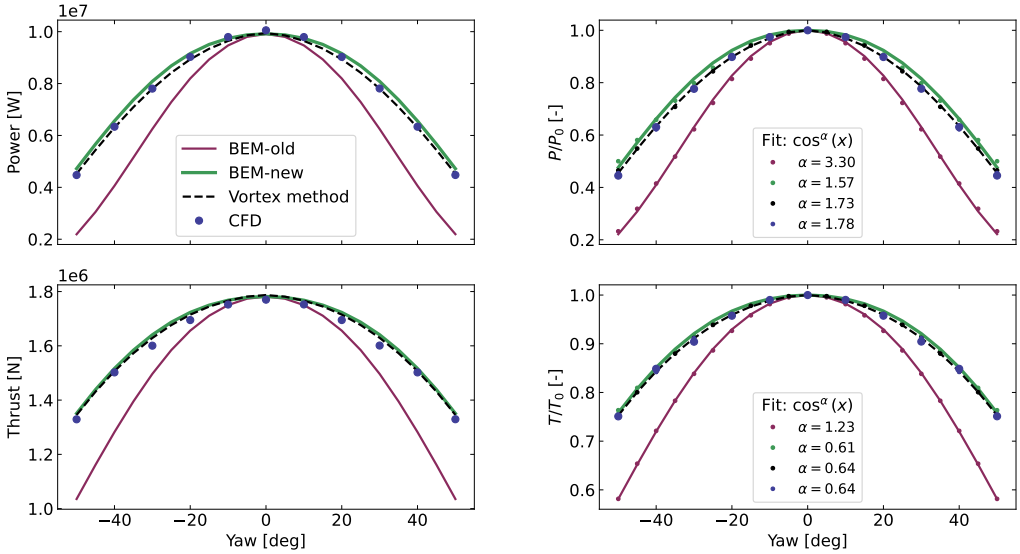

Figure 4. Left: Power and thrust obtained using the old and new AeroDyn implementations, a vortex-based tool, and CFD for a sweep of yaw angles. Right: Same curves but dimensionless. Fits of the form $\cos(\theta_{\text{yaw}})^{\alpha}$ are indicated with dots.

BEM implementation are in disagreement with the other codes. Results from the new BEM implementation, the vortex methods, and the blade-resolved CFD are in strong agreement.

In the right of Figure 4, the results are made dimensionless by dividing with the value at zero yaw. This reduces the impact of potential offsets between the implementations. The dimensionless curves are then fitted with the function $\cos^{\alpha}(\theta_{\text{yaw}})$ to find the exponent α that best match the results in the least-square sense. In this dimensionless representation, the results from the different codes (except BEM-old) strongly agree. The high-fidelity results suggest the following trends at these operating conditions:

$$\frac{P(\theta_{\text{yaw}})}{P(0)} = \cos^{1.75}(\theta_{\text{yaw}}), \qquad \frac{T(\theta_{\text{yaw}})}{T(0)} = \cos^{0.64}(\theta_{\text{yaw}}). \tag{20}$$

The exponents are likely to depend on the operating conditions (see also, [16, 17]) and the turbine design (e.g., in cases of large presweep or precone), and will likely vary for more complex flows (e.g., with shear, veer, turbulence).

Overall, from these results, the new implementation is demonstrating a strong improvement in accuracy over the old BEM implementation of AeroDyn.

4.3. Radial and azimuthal variations

In this section, we illustrate the effect of the new model on the local blade quantities. Figure 5 (left) presents the dimensionless induced velocity normal to the rotor plane, $\boldsymbol{W} \cdot \boldsymbol{n}/U_0$, as obtained by the lifting-line algorithms for three yaw angles: $\theta_{\text{yaw}} = \{-50°, 0°, 50°\}$. The

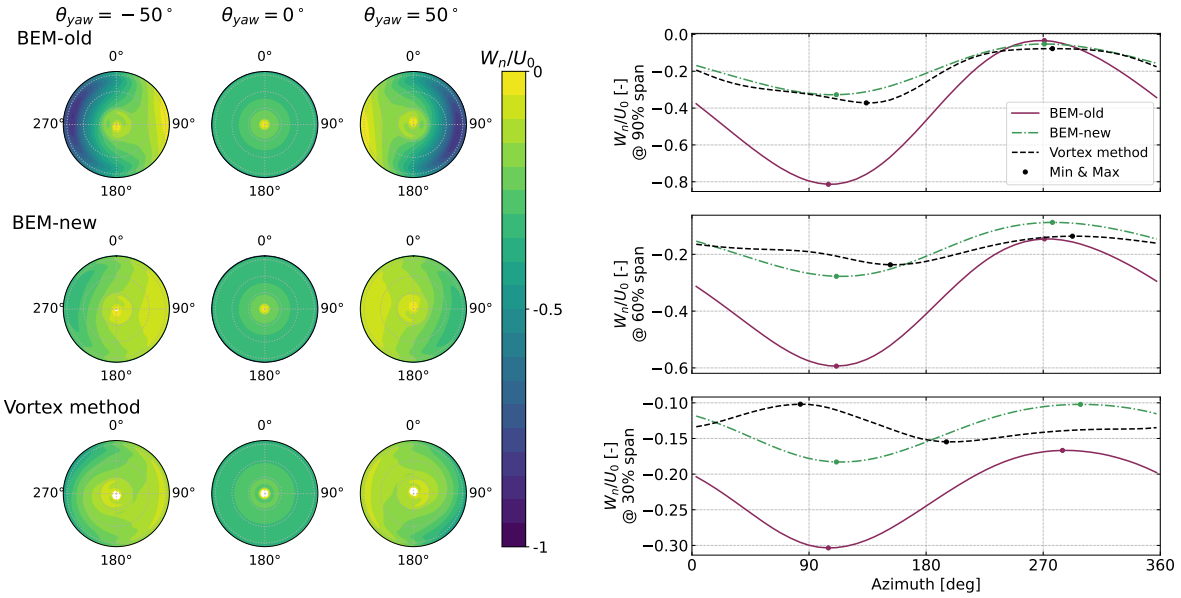

Figure 5. Induced velocity normal to the rotor plane ($\boldsymbol{W} \cdot \boldsymbol{n}$) as obtained by the lifting-line algorithms. Induced velocity is made dimensionless by dividing with U_0. Left: Columns from left to right represent the cases $\theta_{\text{skew}} = \{-50, 0, 50\}°$. The rows are the different algorithms, from top to bottom: BEM-old, BEM-new, and OLAF. Right: Azimuthal variation of the induced velocity at 30%, 60%, and 90% span along the blade for a skew angle of 50°.

algorithms are in strong agreement for zero skew (central column) and the induction profiles are axisymmetric. In skewed conditions, all codes display the expected behavior that the induced velocity is strongest on the side of the rotor plane that is most into the wake ("downwind"). This phenomenon is readily understood by approximating the wake as a collection of vortex rings parallel to the rotor [9, chap.6]. From the figure, we observe that the induced velocities from BEM-old are stronger than those from the other two algorithms. As mentioned in subsection 2.2, the strong induced velocity comes from the lack of skew momentum correction. Qualitatively, the BEM-new results are in fair agreement with the vortex code results and show a clear improvement compared to the previous implementation.

In Figure 5 (right), we plot the azimuthal variation of the induced velocity at three spanwise positions (30%, 60%, 90%) for the case $\theta_{\text{yaw}} = 50°$. We purposely choose a challenging case to highlight differences between BEM and OLAF; these differences are less pronounced for smaller yaw angles (not shown). In this paragraph, we take the OLAF results as a reference because it is of higher fidelity and does not rely on empirical models. We observe that the prediction of the mean induction levels and amplitude ranges are significantly improved using BEM-new compared to BEM-old. We note that the induction redistribution model used in BEM enforces a sinusoidal oscillation of the induction, but we see that OLAF oscillations are flatter and not symmetric with respect to the mean signal. Such differences point to the need for improved induction redistribution models. The azimuthal locations of the minimum and maximum inductions (indicated with • in the figure) are well captured by the BEM codes for the outer part of the blade (60% and 90% span), but not for the inner part of the blade where

a near 180° phase shift is observed. Differences near the root can be related to the swirl in the wake.[4] The lack of modeling of the root vortex is often given as a reason for these differences. Yet the investigation performed in [18] did not confirm this assumption but instead pointed to improvements needed in the induction redistribution model with a better account of the annuli dependency.

5. Conclusions

In this work, we presented changes to the blade element momentum (BEM) algorithm in the AeroDyn module of OpenFAST to improve predictions under skewed inflow conditions. We presented the rationale behind Glauert's skew correction and discussed the different conventions possible for the axial induction factor. We implemented Glauert's skew momentum correction and introduced continuous extension of the model for high-thrust conditions. We verified, using a higher-fidelity vortex method and CFD, that the model greatly improves the BEM prediction in large skew for integral quantities (such as power and thrust) and for local quantities (such as the induced velocity). In this work, and for the operating condition considered ($C_T = 0.78$), we found that the power changes with the skew angle as $\cos^{1.75}(\theta_{\text{skew}})$ and the thrust as $\cos^{0.64}(\theta_{\text{skew}})$, based on average results from LES and vortex methods.

The mean and amplitude of the induced velocities predicted by the new BEM algorithm agree to a high degree with the results from the vortex methods. Yet differences in phases were observed toward the root of the blade, and overall, the sinusoidal variations of the BEM inductions appeared to be simplified compared to the variations observed with the vortex code. Further work is therefore needed to investigate the source of these differences, and future work will focus on the implementation of different induction redistribution models. Further tuning of the model is also envisaged, in particular, to verify the high-thrust corrections in skewed conditions and investigate more complex flows including shear, veer, turbulence and transient yawing.

References

[1] B. Jonkman, R. M. Mudafort, A. Platt, E. Branlard, M. Sprague, J. Jonkman, G. Vijayakumar, M. Buhl, H. Ross, P. Bortolotti, M. Masciola, S. Ananthan, M. J. Schmidt, J. Rood, R. Damiani, N. Mendoza, M. Hall, and R. Corniglion, "Openfast v3.4.1. open-source wind turbine simulation tool, available at `http://github.com/OpenFAST/OpenFAST/`," 2023.

[2] A. Ning, "A simple solution method for the blade element momentum equations with guaranteed convergence," *Wind Energy*, vol. 17, pp. 1327–1345, 2014.

[3] K. Boorsma et al., "Progress in the validation of rotor aerodynamic codes using field data," *Wind Energy Science*, vol. 8, no. 2, pp. 211–230, 2023.

[4] H. Glauert, "A general theory of the autogyro," tech. rep., NACA Reports and Memoranda No. 111, 1926.

[5] W. J. Rankine, "On the mechanical principles of the action of propellers," *Transactions of the Institute of Naval Architects*, vol. 6, p. p13, 1865.

[6] R. Froude, "On the part played in propulsion by differences of fluid pressure," *Transactions of the Institute of Naval Architects*, vol. 30, pp. p390–405, 1889.

[7] H. Glauert, "Airplane propellers, Division L," in *Aerodynamic Theory, Volume IV* (W. F. Durand, ed.), Julius Springer, Berlin, 1935.

[8] H. Glauert, *Elements of Aerofoil and Airscrew Theory*. Cambridge University Press, 1926.

[9] E. Branlard, *Wind Turbine Aerodynamics and Vorticity-Based Methods: Fundamentals and Recent Applications*. Springer International Publishing, 2017.

[10] M. O. L. Hansen, *Aerodynamics of Wind Turbines - Second Edition*. London, Sterling, VA: Earthscan, 2008.

[11] H. A. Madsen, T. J. Larsen, G. R. Pirrung, A. Li, and F. Zahle, "Implementation of the blade element momentum model on a polar grid and its aeroelastic load impact," *Wind energy science*, vol. 1, 2019.

[12] J. Ledoux, S. Riffo, and J. Salomon, "Analysis of the blade element momentum theory," *SIAM Journal on Applied Mathematics*, vol. 81, p. 2596–2621, Jan. 2021.

[4] Drag and separation effects are also significant near the root, but these effects are not fully accounted for by lifting-line codes.

[13] E. Branlard, I. Brownstein, B. Strom, J. Jonkman, S. Dana, and E. I. Baring-Gould, "A multipurpose lifting-line flow solver for arbitrary wind energy concepts," *Wind Energy Science*, vol. 7, no. 2, pp. 455–467, 2022.
[14] M. Sprague, S. Ananthan, G. Vijayakumar, and M. Robinson, "Exawind: A multifidelity modeling and simulation environment for wind energy," *Journal of Physics: Conference Series*, vol. 1452, p. 012071, 01 2020.
[15] E. Gaertner, J. Rinker, L. Sethuraman, F. Zahle, B. Anderson, G. Barter, N. Abbas, F. Meng, P. Bortolotti, W. Skrzypinski, G. Scott, R. Feil, H. Bredmose, K. Dykes, M. Shields, C. Allen, and A. Viselli, "Iea wind tcp task 37: Definition of the iea 15-megawatt offshore reference wind turbine," tech. rep., National Renewable Energy Laboratory, Golden, CO, USA, 3 2020.
[16] H. Madsen, N. N. Sørensen, and S. Schreck, *Yaw Aerodynamics Analyzed with Three Codes in Comparison with Experiment*. 2003.
[17] M. F. Howland, C. M. González, J. J. P. Martínez, J. B. Quesada, F. P. Larrañaga, N. K. Yadav, J. S. Chawla, and J. O. Dabiri, "Influence of atmospheric conditions on the power production of utility-scale wind turbines in yaw misalignment," *Journal of Renewable and Sustainable Energy*, vol. 12, no. 6, p. 063307, 2020.
[18] E. Branlard, M. Gaunaa, and E. Machefaux, "Investigation of a new model accounting for rotors of finite tip-speed ratio in yaw or tilt," *Journal of Physics: Conference Series*, vol. 524, no. 1, pp. 1–11, 2014.

Appendix A. Convention for the axial induction factor

As mentioned in subsection 2.2, different definitions are possible for the axial induction factor and the thrust coefficient. In this section, we formalize these conventions using dedicated notations and illustrate the differences between the two. The axial induction factor may be defined using the wind normal to the rotor, noted a (approach used here, in Equation 5, and in OpenFAST), or using the wind along the "main flow" direction (approach used, e.g., in [11]), noted a_0:

$$\boldsymbol{W} \cdot \boldsymbol{n} = -aU_n = -a_0 U_0, \qquad (\text{with } U_n = U_0 \cos\theta_{\text{skew}}) \tag{A.1}$$

The local thrust, Equation 6, can therefore be expressed as

$$\mathrm{d}T = \frac{\mathrm{d}S}{2}\rho(U_0\cos\theta_{\text{skew}})^2\ 4a\sqrt{(1-a)^2+\tan^2\theta_{\text{skew}}} = \frac{\mathrm{d}S}{2}\rho(U_0)^2\ 4a_0\sqrt{1+a_0^2-2a_0\cos\theta_{\text{skew}}} \tag{A.2}$$

The thrust coefficient can also be defined as a function of U_n (as in Equation 7) or U_0:

$$C_{t,U_n} = \frac{\mathrm{d}T}{\frac{1}{2}\rho\,\mathrm{d}S\,U_n^2}, \qquad C_{t,U_0} = \frac{\mathrm{d}T}{\frac{1}{2}\rho\,\mathrm{d}S\,U_0^2} \tag{A.3}$$

The different conventions above are related as:

$$a_0 = a\cos\theta_{\text{skew}}, \qquad C_{T,U_0} = \cos^2\theta_{\text{skew}}\, C_{T,U_n} \tag{A.4}$$

leading to the following forms, further illustrated in Figure A1:

$$C_{T,U_0} = 4a_0\sqrt{1+a_0^2-2a_0\cos\theta_{\text{skew}}} = \cos^2\theta_{\text{skew}}\ 4a\sqrt{(1-a)^2+\tan^2\theta_{\text{skew}}} \tag{A.5}$$

$$C_{T,U_n} = 4a\sqrt{(1-a)^2+\tan^2\theta_{\text{skew}}} = \frac{1}{\cos^2\theta_{\text{skew}}}\ 4a_0\sqrt{1+a_0^2-2a_0\cos\theta_{\text{skew}}} \tag{A.6}$$

We note that the "U_0" convention has the advantage that the axial induction is well defined, even for skew angles of 90°. The main disadvantage of this convention is that the choice of flow direction at a given blade node may be difficult in simulations with turbulence. The opposite is true for the "U_n" convention: the direction is well defined (normal to the rotor), but, for a skew angle of 90°, U_n is 0 and it is therefore impossible to retrieve the induced velocity normal to the disk using an axial induction factor. For both conventions, the choice of which amplitude to use (e.g., the velocity at the blade node or in a weighted sector) in sheared and turbulent simulations adds complexity to these conventions.

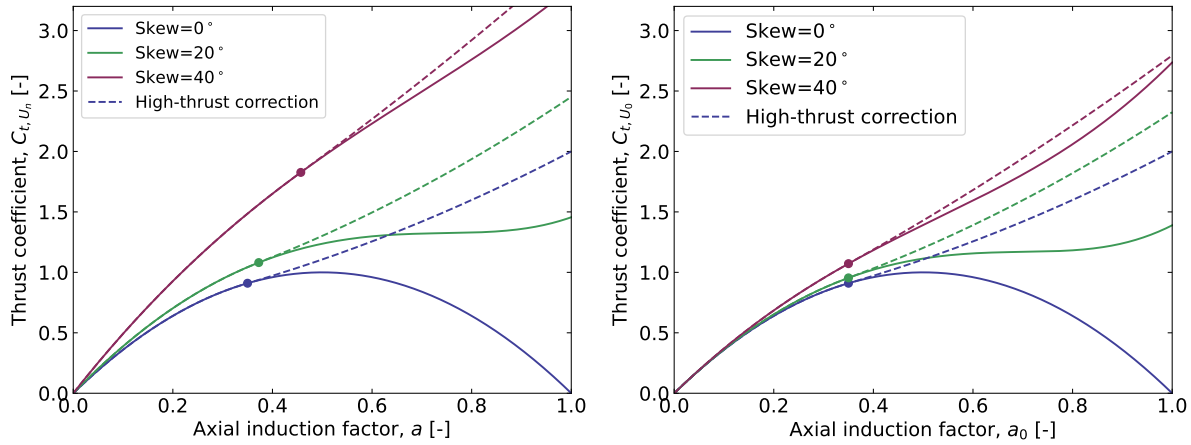

Figure A1. Skew momentum relationship for two conventions of C_t and a. Left: $C_{t,U_n}(a)$. Right: $C_{t,U_0}(a_0)$. The different variables are defined in Equation A.1 and Equation A.3.

Acknowledgements
This work was authored in part by the National Renewable Energy Laboratory, operated by Alliance for Sustainable Energy, LLC, for the U.S. Department of Energy (DOE) under Contract No. DE-AC36-08GO28308. Funding provided by the U.S. Department of Energy Office of Energy Efficiency and Renewable Energy Wind Energy Technologies Office. The views expressed in the article do not necessarily represent the views of the DOE or the U.S. Government. The U.S. Government retains and the publisher, by accepting the article for publication, acknowledges that the U.S. Government retains a nonexclusive, paid-up, irrevocable, worldwide license to publish or reproduce the published form of this work, or allow others to do so, for U.S. Government purposes.